Computational Predictions on the Magnetic Particle Imaging Performance of Tracers Subjected to Magnetic Dipole–Dipole Interactions

Ebrahim Azizi[1], Shahriar Mostufa[1], Bahareh Rezaei[1], Shumin Xin[2], Jiajia Sun[2], Zongqian Shi[2], Jenifer Gómez-Pastora[3], and Kai Wu[1]

[1]Department of Electrical and Computer Engineering, Texas Tech University, Lubbock, TX 79409 USA
[2]State Key Laboratory of Electrical Insulation and Power Equipment, Xi'an Jiaotong University, Xi'an, Shaanxi 710049, China
[3]Department of Chemical Engineering, Texas Tech University, Lubbock, TX 79409 USA

Magnetic particle imaging (MPI) is a tracer-based tomographic imaging technique recognized for its tissue-depth-independent sensitivity, quantitative accuracy, and high spatial and temporal resolution. Superparamagnetic iron oxide nanoparticle (SPION) tracers are widely used in MPI research for applications such as cancer imaging, cardiovascular imaging, stem cell tracking, drug delivery monitoring. As MPI transitions toward clinical use, several challenges remain to be addressed, including tracer design, image reconstruction algorithms, and optimized field configurations, to achieve improved imaging performance. The magnetic dipole–dipole interactions (dipolar interactions) between magnetized tracers are often overlooked in applications such as magnetic sensing, imaging, and separation. However, in imaging scenarios where tracers target tumors, stem cells, or similar applications, surface-functionalized tracers tend to aggregate at target sites, leading to reduced interparticle distances where dipolar fields from neighboring tracers become significant. This study investigates the impact of magnetic dipolar interactions among SPION tracers on MPI imaging performance by tuning the inter-particle distances. Using the stochastic Langevin function, we modeled an ensemble of 1000 SPION tracers within a field-free region (FFR). Key magnetization dynamics such as time-domain magnetization responses, magnetization-field response (M–H) curves, voltage signals recorded by receiver coils, higher harmonics, and point spread functions (PSFs) were analyzed. Here, higher harmonics and the full width at half maximum (FWHM) of the PSFs serve as indicators for evaluating the impact of dipolar interactions on MPI performance.

***Index Terms*— Dipole–dipole field, dynamic magnetic response, magnetic particle imaging (MPI), point-spread function (PSF), superparamagnetic iron oxide nanoparticle (SPION).**

I. Introduction

IN RECENT years, magnetic particle imaging (MPI) has emerged as a promising candidate for safer, higher-contrast, and higher-resolution tomographic imaging techniques that could potentially be translated into clinical settings soon. Studies by [1], [2], [3], and [4] state that MPI is a tracer-based imaging technique, similar to positron emission tomography (PET), but it utilizes superparamagnetic iron oxide nanoparticle (SPION) tracers that are radiation-free and biologically safe [5]. The superparamagnetic properties of SPION tracers ensure their colloidal stability in liquid and prevent clustering in both in vitro and in vivo applications. The combination of SPION tracers and the MPI system offers numerous advantages, including biocompatibility, high imaging resolution, and compatibility with other biological imaging systems, making it highly appealing and valuable to researchers and various biomedical fields [6], [7], [8]. For example, in MPI-based tumor imaging, SPION tracers are typically functionalized with ligands to enhance tumor-targeting efficiency as stated by Tay et al. [5], Yu et al. [9], and Arami et al. [10]. When these tracers accumulate in the tumor region, the interparticle distance decreases, and the magnetic dipole–dipole interactions become significant. This magnetic dipolar field, along with the excitation field, gradient field, and focus field, collectively act on SPION tracers and modulate their dynamic magnetization responses [11], [12], [13], [14].

Extensive research has been conducted on MPI modeling to optimize input parameters such as particle anisotropy, relaxation phenomena, excitation field properties, and more [15], [16], [17], [18], [19]. In most MPI modeling works, these interparticle interactions are often ignored, which diminishes the accuracy of the models. Herein, we applied a stochastic Langevin function [20], [21], [22], [23] with combined Brownian and Néel relaxations to model the collective dynamic magnetizations of an ensemble of 1000 SPION tracers with varying degrees of dipole–dipole interactions (i.e., varying interparticle distances and dipolar fields). We study how this dipolar field affects MPI performance by observing the time-domain magnetization responses, dynamic magnetization-field curves (M–H curves), voltage signals recorded by the receiver coils, higher harmonics, and point-spread functions (PSFs). We report that at shorter interparticle distances, stronger dipolar interactions significantly reduce magnetizations of tracers. As the distance between tracers increases, tracer magnetization rises, and beyond a critical distance, the dynamic field—comprising the excitation field and anisotropy energy—becomes a dominant factor influencing tracers' magnetization dynamics. At distances beyond this critical point, the impact of the dipolar field on magnetization dynamics becomes negligible, leaving the dynamic field as the primary driver.

Received 11 November 2024; revised 26 January 2025; accepted 31 January 2025. Date of publication 4 February 2025; date of current version 27 August 2025. Corresponding author: K. Wu (e-mail: kai.wu@ttu.edu).

Color versions of one or more figures in this article are available at https://doi.org/10.1109/TMAG.2025.3538580.

Digital Object Identifier 10.1109/TMAG.2025.3538580

II. Mathematical Models

The magnetization dynamics of an ensemble of noninteracting SPION tracers in a viscous medium can be described by the Landau–Lifshitz–Gilbert (LLG) in the following equation:

$$\tau_0 \frac{d\boldsymbol{m}}{dt} = \left(\frac{1}{\alpha}\boldsymbol{\xi} + \boldsymbol{m} \times \boldsymbol{\xi} + \frac{1}{\alpha}\boldsymbol{H_{th}} + \boldsymbol{m} \times \boldsymbol{H_{th}}\right) \times \boldsymbol{m} \quad (1)$$

where $\tau_0 = ((\mu(1+\alpha^2))/2k_BT\alpha\gamma)$ known as the Néel attempting time, α is the damping parameter, γ is the electron gyromagnetic ratio, $\mu = M_sV_c$ is one particle magnetic moment, $\boldsymbol{m}$ is the unit magnetization vector, $\boldsymbol{\xi} = (\mu_0\mu\boldsymbol{H}/2k_BT) + \sigma(\boldsymbol{m}\cdot\boldsymbol{n})\boldsymbol{n} + \boldsymbol{H_d}$ is the effective dimensionless dynamic field, $\boldsymbol{H_{th}}$ is the stochastic thermal field with a Gaussian correlation as $\langle \boldsymbol{H}^i_{\boldsymbol{th}}(t)\boldsymbol{H}^j_{\boldsymbol{th}}(t')\rangle = \tau_0\delta_{ij}\delta(t-t')$, μ_0 is vacuum permeability, $\boldsymbol{H}$ is the excitation field, σ is dimensionless magnetic anisotropy, and the effective dimensionless dipolar field $\boldsymbol{H_d} = (\mu_0\mu/2k_BT)\sum_i(\mu_i/4\pi r_i^3)(3(\boldsymbol{m}_i\cdot\boldsymbol{r}_i)\boldsymbol{r}_i - \boldsymbol{r}_i)$ where $\boldsymbol{r}_i$ is the unite vector represents the field direction. The dimensionless anisotropy energy is defined as $\sigma = (K_aV_c/k_BT)$, where K_a is the anisotropy constant and is assumed to be uniaxial, V_c is the magnetic core size, k_B is the Boltzmann's constant, and T is temperature.

The Néel attempt time (τ_0) is a component of the Néel relaxation time and is a function of ac and dc fields, anisotropy, and saturation magnetization $\tau_N = \tau_0 f(M_s, \sigma, H)$, depending on whether the tracers are in equilibrium or nonequilibrium states. Although no comprehensive formulation for this relaxation time has been established, various approaches are discussed in [16], [19], [24], and [25].

Equation (1) is coupled with the differential equation described by the generalized torque applied to the easy axis unit vector $\boldsymbol{n}$ and denoted by (2) when the acceleration is ignored as the tracers' motion is dominant by the viscosity force

$$\tau_B \frac{d\boldsymbol{n}}{dt} = -(\sigma(\boldsymbol{m}\cdot\boldsymbol{n})(\boldsymbol{m}\times\boldsymbol{n}) + \boldsymbol{\theta}_{\text{th}}) \times \boldsymbol{n} \quad (2)$$

where $\boldsymbol{\theta}$ is the effective torque, $\tau_B = (3\eta V_h/2k_BT)$ is the Brownian relaxation time, η is the viscosity, V_h is the hydrodynamic volume of the SPION tracer, and $\boldsymbol{\theta}_{\text{th}}$ is the thermal random torque with Gaussian distribution as $\langle \boldsymbol{\theta}^i_{\boldsymbol{th}}(t)\boldsymbol{\theta}^j_{\boldsymbol{th}}(t')\rangle = \tau_B\delta_{ij}\delta(t-t')$. The effective torque and applied field can be described by the typical Stoner–Wohlfarth prescription.

Since the dipolar field, $\boldsymbol{H_d}$, decreases with the cube of the interparticle distance. Our previous work has shown that the dipolar field becomes negligible at an interparticle distance of 250 nm as demonstrated as Wu et al. [11]. Therefore, in this study, we limit our consideration of dipolar interactions between SPION tracers to a maximum interparticle distance of 250 nm. We varied the interparticle distances from 25 to 250 nm by fixing these SPION tracers at different sets of spatial locations. Then the effective dipolar field, $\boldsymbol{H_d}$, that acts on each SPION tracer is computed and added to the effective field. The coupled stochastic differential equations are simultaneously solved, and the dynamic magnetizations of tracers are sampled at a 5 MHz sampling frequency during three periods of the excitation field. Without the loss of generality, we consider the excitation field is applied along the z-direction and the averaged magnetization of tracers along the z-direction is calculated by $\boldsymbol{M}_z = M_s\overline{\boldsymbol{m}}_z$, where M_s is the saturation of magnetization, and $\overline{\boldsymbol{m}}_z$ is the averaged z-component of the unit magnetization vector over 1000 SPION tracers.

TABLE I
Variables and Values Used in This Work

Variable	Values	Ref.
Viscosity (mPa·s)	1	-
Temperature (K)	300	-
Damping parameter	1	[23]
Gyromagnetic Ratio (GHz/T)	176	[27]
Magnetic Anisotropy K_a (kJ/m^3)	3	[1], [28], [29]
Saturation Magnetization M_s (kA/m)	480	
MNP Core Diameter D_c (nm)	25, 30, 35	-
MNP Hydrodynamic Diameter D_h (Surface coating layer thickness of 10 nm)	D_h=D_c+10	-
Interparticle Distance d (nm)	25 nm - 250 nm	-
Excitation Field Amplitude (mT/μ_0)	20	[1], [3]
Excitation Field Frequency (kHz)	25	

Given the high computational demands of calculating dipolar fields generated by neighboring tracers, we limited our simulation to 1000 SPION tracers, which resulted in an output magnetization with a high noise level. To address this, a Butterworth low-pass filter with a cutoff frequency at 375 kHz and a forward-backward digital filter to eliminate phase delay was applied. Further smoothing is applied by the Savitzky–Golay filter, and edge defects are encountered by Kaiser windowing process. Results were analyzed over time with the M–t curve and over the field with the M–H curves. The M–t curves were further processed to calculate the time-domain signal. In this work, we assumed an ensemble of 1000 SPION tracers inside the field-free region (FFR), where these tracers were modeled with a delta distribution. Finally, Faraday's law of induction was applied to determine the time-domain voltage generated by the tracers

$$u(t) = -Np_c\mu\frac{\partial M(r_{\text{ffp}}, t)}{\partial t} \quad (3)$$

where N is the number of SPION tracers, p_c is the coil sensitivity (we used 1 mT/A based on experimentally observed values), Δv is the FFP volume, and r_{ffp} sets as the voxel's center.

The time-domain voltage is further analyzed using the fast Fourier transform (FFT) to identify the higher harmonic components. This time-domain assessment of magnetization provides the signal-to-noise ratio (SNR) of the resulting harmonics. Conversely, the M–H curve is analyzed to calculate the point spread function (PSF) and the full width at half maximum (FWHM), which is directly related to the intrinsic spatial resolution in MPI [26]

$$\Delta x = \frac{k_BT}{\mu_0\mu G}\xi_{\text{FWHM}} \quad (4)$$

where G represents the gradient field strength and ξ_{FWHM} denotes the FWHM.

Additional parameters used in the simulation are listed in Table I.

III. Results and Discussion

A. Effect of Dipole–Dipole Interactions on MPI Performance of 25 nm SPION Tracers

We modeled the dynamic magnetization of an ensemble of SPION tracers with 25 nm core sizes subjected to an excitation field. The magnetization of the tracers along the excitation

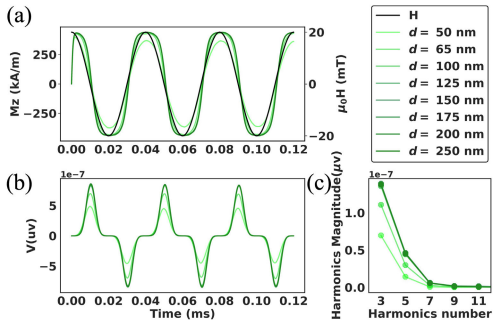

Fig. 1. Magnetic responses of 25 nm core size SPION tracers separated at different interparticle distances. (a) Magnetization responses. (b) Voltage signals recorded by the receiver coil. (c) Harmonic amplitudes.

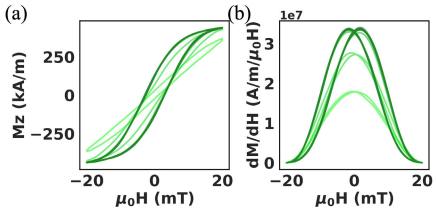

Fig. 2. Magnetic responses of 25 nm core size SPION tracers separated at different interparticle distances. (a) M–H curves. (b) PSFs.

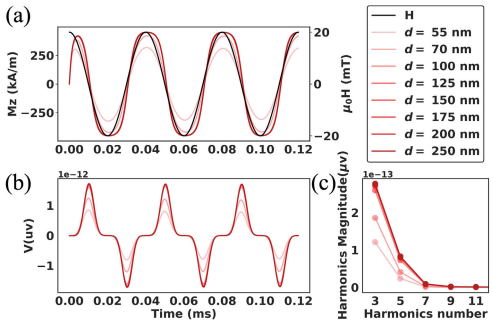

Fig. 3. Magnetic responses of 30 nm core size SPION tracers separated at different interparticle distances. (a) Magnetization responses. (b) Voltage signals recorded by the receiver coil. (c) Harmonic amplitudes.

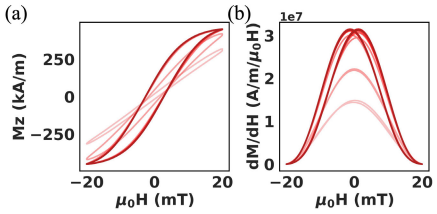

Fig. 4. Magnetic responses of 30 nm core size SPION tracers separated at different interparticle distances. (a) M–H curves. (b) PSFs.

field direction was recorded in the time domain and plotted in Fig. 1(a) for varying interparticle distances ranging from 50 to 250 nm.

As the interparticle distance increases, the maximum magnetization amplitude grows, transitioning from a sinusoidal-like to a square-like shape [Fig. 1(a)]. This results in higher voltage signals and harmonic amplitudes, as shown in Fig. 1(b) and (c). At shorter interparticle distances, the M–H curve exhibits a more linear behavior with a small hysteresis loop, indicating that dipolar interactions dominate over Néel relaxation. In contrast, at longer distances, the M–H curve becomes nonlinear, tracers achieve saturation magnetization, and Néel relaxation produces a wider hysteresis loop. Beyond the critical interparticle distance of 100 nm, where dipolar interactions become negligible, magnetization stabilizes and shows no significant changes with further increases in distance [Fig. 2(a)]. Similarly, the PSF exhibits lower peaks when particles are closer together. The peaks increase with interparticle distance, reaching a maximum at around 100 nm, where the dipolar field has minimal effect. Beyond this point, the PSF remains unchanged.

This effect arises from the contribution of dipolar fields ($\boldsymbol{H_d}$) on the dimensionless field $\boldsymbol{\xi}$. At small interparticle distances, the dipolar field dominates over the excitation and anisotropy fields, resulting in weak magnetization. As the interparticle distance increases, the dipolar field weakens, thus, the excitation and anisotropy fields become prominent. At an interparticle distance of 100 nm, the effect of the dipolar field is minimal, and beyond this point, the magnetization behavior is entirely governed by the excitation and anisotropy fields.

B. Effect of Dipole–Dipole Interactions on MPI Performance of 30 nm SPION Tracers

Like the 25 nm core size SPION tracers, the dynamic magnetization responses of 30 nm core size SPION tracers show low amplitudes and sinusoidal shapes at short interparticle distances (d = 55 and 70 nm). This results in weaker voltage signals and lower harmonic amplitudes. With increased interparticle distances, the magnetization amplitude rises, yielding stronger voltage signals and higher harmonic amplitudes [Fig. 3(b) and (c)]. For sufficiently long interparticle distances where the field that governs magnetization dynamics is the dynamic field $\boldsymbol{\xi}$ and the dipolar field is small, the M–t curve shows a larger phase delay to the excitation field compared to the 25 nm SPOINs due to the larger core sizes and increased Néel relaxation time [Fig. 3(a)]. The voltage signals and harmonic amplitudes from the 30 nm SPION tracers are slightly higher than 25 nm SPION tracers due to the increased core size.

The M–H curves collected from these 30 nm SPION tracers also reflect this behavior: with increasing interparticle distances, the dipolar disturbance decreases, allowing tracers to approach their saturation magnetizations. This critical interparticle distance is at around 125 nm [Fig. 4(a)], different from the 100 nm distance for 25 nm SPION tracers. This change originates from the larger SPION tracer size.

The PSF profiles show smaller FWHM values at shorter interparticle distances due to stronger dipolar interactions from larger magnetic moments. At longer interparticle distances, FWHM decreases slightly as the tracers reach full saturation [Fig. 4(a)]. This indicates that the excitation field becomes dominant, reducing phase delay in the magnetization response, even with longer Néel relaxation times due to the larger particle size.

C. Effect of Dipole–Dipole Interactions on MPI Performance of 35 nm SPION Tracers

SPION tracers with 35 nm core sizes exhibit low magnetization at shorter interparticle distances, similar to those with 25 and 30 nm cores. As the interparticle distance increases, magnetization becomes more pronounced, causing the voltage signal to transition from a low-amplitude sinusoidal shape

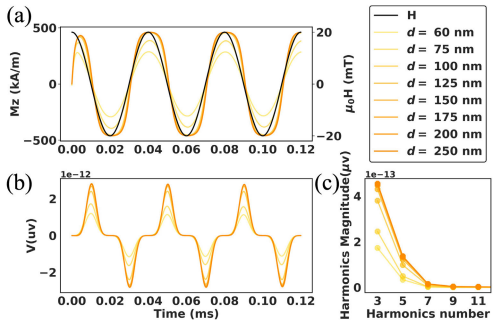

Fig. 5. Magnetic responses of 35 nm core size SPION tracers separated at different interparticle distances. (a) Magnetization responses. (b) Voltage signals recorded by the receiver coil. (c) Harmonic amplitudes.

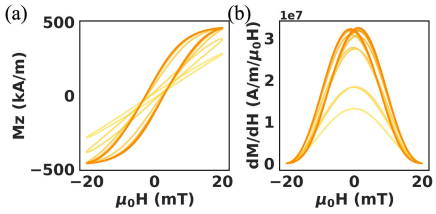

Fig. 6. Magnetic responses of 35 nm core size SPION tracers separated at different interparticle distances. (a) M–H curves. (b) PSFs.

to a higher-amplitude, square-like shape [Fig. 5(a) and (b)]. This transition is accompanied by increased nonlinearity in the magnetization response and higher harmonic amplitudes [Fig. 5(c)]. At shorter interparticle distances, the M–H curves are linear with narrow hysteresis loops. With increasing interparticle distance, the curves become nonlinear, eventually reaching full saturation, similar to SPION tracers with 30 nm cores [Fig. 6(a)].

The PSF follows a similar trend as SPION tracers with 30 nm, showing lower peaks at shorter interparticle distances and higher peaks as the distance increases [Fig. 6(b)]. Due to the larger tracer core size as well as higher magnetic moment per tracer particle, the critical interparticle distance at which the dipolar field no longer significantly affects tracers' dynamic magnetizations is observed at 150 nm. Beyond this point, the excitation and anisotropy fields dominate particle dynamics.

IV. Conclusion

In this study, we employed the stochastic Langevin function to investigate the effect of dipole–dipole interactions of tracers on the MPI imaging performance. We considered 1000 SPION tracers with 25, 30, and 35 nm core sizes and obtained their magnetization responses under the excitation field of 25 kHz frequency and 20 mT/μ_0 amplitude. We further considered low-pass filter with magnetization at the 375 kHz cut-off frequency and forward-backward digital filter. The 375 kHz cut-off frequency ensures that harmonics below the 15th remain undisturbed, while the forward-backward digital filter eliminates any phase delay introduced during filtering. The filtered magnetization is evaluated in the time domain by the M–t curve, voltage signals, and in the frequency domain by harmonic amplitudes that give an intuition of SNR. Moreover, it is evaluated in the excitation field by the M–H curve and PSF that gives the imaging resolution. Prior to the time and field evaluation of magnetization, we applied a Kaiser window between two subsequent saturation points to avoid the large magnetization ratios at saturation points and decrease the effect of side lobes in the frequency domain. Furthermore, Savitzky–Golay filtering is applied to reduce the residual high-frequency noises that remain after low-pass filtering and become critical in derivatives.

TABLE II
Summary of FWHM Under Different Interparticle Distances for Different SPOIN Tracers

Tracer Core Size	Inter-particle Distance	FWHM (mT/μ_0)
25 nm	50 nm	19.806
	65 nm	18.155
	100 nm	15.866
	125 nm	15.866
	150 nm	16.426
	175 nm	15.835
	200 nm	16.426
	250 nm	16.426
30 nm	55 nm	20.357
	70 nm	19.265
	100 nm	16.450
	125 nm	15.866
	150 nm	15.866
	175 nm	15.866
	200 nm	15.866
	250 nm	15.866
35 nm	60 nm	20.357
	75 nm	19.806
	100 nm	17.595
	125 nm	16.450
	150 nm	16.450
	175 nm	15.866
	200 nm	15.866
	250 nm	15.866

We used the harmonics of magnetization responses as a metric for imaging quality [Figs. 1(c), 3(c), and 5(c)] and FWHM as a measure of imaging resolution. The FWHM values, derived from the PSF [Figs. 2(b), 4(b), and 6(b)], are summarized in Table II.

For the 25 nm SPOINs, decreasing interparticle distances leads to reduced magnetization amplitude and weaker MPI signal due to the intensified dipolar field, which restricts tracer magnetization. At longer interparticle distances (over 100 nm, see Table II), the dipolar field weakens, allowing the dynamic field to dominate and result in enhanced magnetization and signal harmonics. Beyond this distance, the dipolar field becomes negligible, allowing the tracers to reach saturation magnetization while still contributing to anisotropy. However, the saturation magnetization is relatively lower compared to SPION tracers with 30 and 35 nm cores due to the smaller core size. The smaller core size also leads to a faster reduction of the dipolar field at larger distances.

For the 30 nm SPION tracers, the patterns in magnetization, voltage signals, and harmonics are like those observed from the 25 nm SPION tracers. However, the M–t curves exhibit a larger phase delay to the excitation field, attributed to the larger core size. Voltage signal peaks increase with interparticle distance up to a critical distance (125 nm, see Table II), after which they remain constant. The harmonic amplitudes are slightly higher than those of 25 nm SPION tracers due to the larger core size. Harmonics below the ninth show increased

amplitudes at larger interparticle distances, although they still decrease monotonically with increasing harmonic order, with a sharp drop occurring at the ninth harmonic. The M–H curve transitions from linear magnetization with narrow hysteresis to full saturation at around 125 nm interparticle distance and remains constant beyond this distance. Similarly, the PSF peaks increase to maximum amplitude at 125 nm and remain unchanged thereafter. The transition to higher magnetization responses, voltage amplitudes, and harmonics with increasing interparticle distance is more gradual for 30 nm SPION tracers compared to 25 nm tracers. This is due to the larger core sizes being more strongly influenced by the dipolar field than smaller cores when evaluated at the same observation distance.

For a core size of 35 nm, the general trends in M–t curves, voltage signals, harmonics, M–H curves, and PSF remain consistent, with some variations. The M–t curves exhibit a slight phase delay, attributed to the increased Néel relaxation time and core size. The peak voltage signals increase more gradually than the 25 and 30 nm tracers due to the larger core size having more sense of interparticle distances and becoming more influential at the same observation points. Harmonics show a slight increase due to the larger core size. The maximum magnetization in M–H curves increases, approaching the saturation magnetization point. This increase continues until it peaks at a critical interparticle distance of 150 nm, after which it remains constant. The PSF remains largely unaffected in fields where the dipolar field has minimal influence on magnetization dynamics. For this core size, the dipolar field becomes negligible at a distance of 150 nm (Table II), beyond which the magnetization dynamics, voltage signals, harmonics, M–H curves, and FWHM values remain unchanged.

ACKNOWLEDGMENT

The work of Bahareh Rezaei was supported by the Distinguished Graduate Student Assistantships (DGSAs) offered by Texas Tech University. The work of Kai Wu was supported by Texas Tech University through Higher Education Funds (HEF) New Faculty Start-Up, National Research University Fund (NRUF) Start-Up, and Core Research Support Fund.

Kai Wu thanks Dr. John B. Weaver of Dartmouth College for helpful discussions.

REFERENCES

[1] K. Wu et al., "Roadmap on magnetic nanoparticles in nanomedicine," *Nanotechnology*, vol. 36, no. 4, Jan. 2025, Art. no. 042003, doi: 10.1088/1361-6528/ad8626.

[2] B. Rezaei et al., "Magnetic nanoparticles for magnetic particle imaging (MPI): Design and applications," *Nanoscale*, vol. 16, no. 25, pp. 11802–11824, 2024, doi: 10.1039/d4nr01195c.

[3] T. Knopp and T. M. Buzug, *Magnetic Particle Imaging: An Introduction to Imaging Principles and Scanner Instrumentation*. Cham, Switzerland: Springer, 2012.

[4] T. Knopp, N. Gdaniec, and M. Möddel, "Magnetic particle imaging: From proof of principle to preclinical applications," *Phys. Med. Biol.*, vol. 62, no. 14, pp. R124–R178, Jun. 2017, doi: 10.1088/1361-6560/aa6c99.

[5] Z. W. Tay et al., "Magnetic particle imaging: An emerging modality with prospects in diagnosis, targeting and therapy of cancer," *Cancers*, vol. 13, no. 21, p. 5285, Oct. 2021, doi: 10.3390/cancers13215285.

[6] X. Xie et al., "Magnetic particle imaging: From tracer design to biomedical applications in vasculature abnormality," *Adv. Mater.*, vol. 36, no. 17, Apr. 2024, Art. no. 2306450, doi: 10.1002/adma.202306450.

[7] F. Thieben et al., "System characterization of a human-sized 3D real-time magnetic particle imaging scanner for cerebral applications," *Commun. Eng.*, vol. 3, no. 1, p. 47, Mar. 2024.

[8] W. Yang et al., "Quantitative visualization of myocardial ischemia-reperfusion-induced cardiac lesions via ferroptosis magnetic particle imaging," *Theranostics*, vol. 14, no. 3, pp. 1081–1097, 2024.

[9] E. Y. Yu et al., "Magnetic particle imaging: A novel in vivo imaging platform for cancer detection," *Nano Lett.*, vol. 17, no. 3, pp. 1648–1654, Mar. 2017.

[10] H. Arami et al., "Tomographic magnetic particle imaging of cancer targeted nanoparticles," *Nanoscale*, vol. 9, no. 47, pp. 18723–18730, Dec. 2017, doi: 10.1039/C7NR05502A.

[11] K. Wu, D. Su, R. Saha, J. Liu, and J.-P. Wang, "Investigating the effect of magnetic dipole–dipole interaction on magnetic particle spectroscopy: Implications for magnetic nanoparticle-based bioassays and magnetic particle imaging," *J. Phys. D, Appl. Phys.*, vol. 52, no. 33, Aug. 2019, Art. no. 335002.

[12] D. Eberbeck and L. Trahms, "Experimental investigation of dipolar interaction in suspensions of magnetic nanoparticles," *J. Magn. Magn. Mater.*, vol. 323, no. 10, pp. 1228–1232, May 2011.

[13] K. Them, "On magnetic dipole–dipole interactions of nanoparticles in magnetic particle imaging," *Phys. Med. Biol.*, vol. 62, no. 14, pp. 5623–5639, Jun. 2017.

[14] N. Gehrke et al., "Magnetic characterization of clustered core magnetic nanoparticles for MPI," *IEEE Trans. Magn.*, vol. 51, no. 2, pp. 1–4, Feb. 2015, doi: 10.1109/TMAG.2014.2358275.

[15] L. R. Croft et al., "Low drive field amplitude for improved image resolution in magnetic particle imaging: Low drive field amplitude for improved image resolution," *Med. Phys.*, vol. 43, no. 1, pp. 424–435, Dec. 2015, doi: 10.1118/1.4938097.

[16] R. J. Deissler, Y. Wu, and M. A. Martens, "Dependence of Brownian and Néel relaxation times on magnetic field strength," *Med. Phys.*, vol. 41, no. 1, Jan. 2014, Art. no. 012301, doi: 10.1118/1.4837216.

[17] C. Kuhlmann et al., "Drive-field frequency dependent MPI performance of single-core magnetite nanoparticle tracers," *IEEE Trans. Magn.*, vol. 51, no. 2, pp. 1–4, Feb. 2015.

[18] C. Saayujya et al., "Pulsed MPI relaxometry of Brownian and Néel field-dependent relaxation in superparamagnetic magnetite nanoparticles confirm theory and simulations," *Small*, vol. 20, no. 44, Nov. 2024, Art. no. 2403283, doi: 10.1002/smll.202403283.

[19] T. Yoshida and K. Enpuku, "Field-dependent Néel relaxation time of magnetic nanoparticles in AC excitation fields: Boundary field between Néel- and Brownian-dominant regions," *J. Appl. Phys.*, vol. 135, no. 9, Mar. 2024, Art. no. 093901. Accessed: Dec. 22, 2024. [Online]. Available: https://pubs.aip.org/aip/jap/article/135/9/093901/3268017

[20] N. A. Usov and B. Y. Liubimov, "Dynamics of magnetic nanoparticle in a viscous liquid: Application to magnetic nanoparticle hyperthermia," *J. Appl. Phys.*, vol. 112, no. 2, Jul. 2012, Art. no. 023901.

[21] S. A. Shah, D. B. Reeves, R. M. Ferguson, J. B. Weaver, and K. M. Krishnan, "Mixed Brownian alignment and Néel rotations in superparamagnetic iron oxide nanoparticle suspensions driven by an AC field," *Phys. Rev. B, Condens. Matter*, vol. 92, no. 9, Sep. 2015, Art. no. 094438.

[22] D. B. Reeves and J. B. Weaver, "Simulations of magnetic nanoparticle Brownian motion," *J. Appl. Phys.*, vol. 112, no. 12, Dec. 2012, Art. no. 124311.

[23] D. B. Reeves and J. B. Weaver, "Combined Néel and Brown rotational Langevin dynamics in magnetic particle imaging, sensing, and therapy," *Appl. Phys. Lett.*, vol. 107, no. 22, Nov. 2015, Art. no. 223106.

[24] A. E. Deatsch and B. A. Evans, "Heating efficiency in magnetic nanoparticle hyperthermia," *J. Magn. Magn. Mater.*, vol. 354, pp. 163–172, Mar. 2014.

[25] J. Dieckhoff, D. Eberbeck, M. Schilling, and F. Ludwig, "Magnetic-field dependence of Brownian and Néel relaxation times," *J. Appl. Phys.*, vol. 119, no. 4, Jan. 2016, Art. no. 043903. Accessed: Jan. 7, 2025. [Online]. Available: https://pubs.aip.org/aip/jap/article/119/4/043903/142688

[26] J. Rahmer, J. Weizenecker, B. Gleich, and J. Borgert, "Signal encoding in magnetic particle imaging: Properties of the system function," *BMC Med. Imag.*, vol. 9, no. 1, p. 4, Dec. 2009.

[27] T. Kluth, "Mathematical models for magnetic particle imaging," *Inverse Problems*, vol. 34, no. 8, Aug. 2018, Art. no. 083001, doi: 10.1088/1361-6420/aac535.

[28] K. Wu, D. Su, J. Liu, R. Saha, and J.-P. Wang, "Magnetic nanoparticles in nanomedicine: A review of recent advances," *Nanotechnology*, vol. 30, no. 50, Dec. 2019, Art. no. 502003.

[29] K. Wu et al., "Magnetic nanoparticles and magnetic particle spectroscopy-based bioassays: A 15 year recap," *Nano Futures*, vol. 6, no. 2, Jun. 2022, Art. no. 022001.